Combustion and Flame 236 (2022) 111813

Contents lists available at ScienceDirect

Combustion and Flame

journal homepage: www.elsevier.com/locate/combustflame

Tailoring the gain and phase of the flame transfer function through targeted convective-acoustic interference

Eirik Æsøy*, Håkon T. Nygård, Nicholas A. Worth, James R. Dawson

Department of Energy and Process Engineering, Norwegian University of Science and Technology, Trondheim N-7491, Norway

ARTICLE INFO

Article history:
Received 29 June 2021
Revised 10 October 2021
Accepted 11 October 2021

Keywords:
Hydrogen
Thermoacoustic instability
Flame transfer function
Flame dynamics

ABSTRACT

This paper investigates how targeted interference between two well characterized sources of hydrodynamic disturbances can modify the response of premixed bluff body stabilised H_2/CH_4 flames with and without swirl. We introduce modulations into the Flame Transfer Function (FTF) through hydrodynamic interference between the shedding of vortices/wakes from different shaped bodies upstream of the flame and the vortex roll-up at the flame base caused by acoustic forcing. By placing a set of small diameter cylinders, a streamlined body, or a swirler upstream of the bluff body and varying the distance from the dump plane, the gain and phase of the FTFs could be modulated at targeted frequencies providing a method to suppress thermoacoustic instabilities. We further investigate the flame response which shows that modulations in the fluctuating global heat release rate are caused by linear superposition along the flame front. At frequencies leading to destructive interference, large-scale wrinkling of the flame front occurs which increases the flame surface area but is offset by the simultaneous pinch-off of the flame tip which decreases flame surface area. Their combined effect reduces the amplitude of the fluctuating global heat release rate. At frequencies of constructive interference, large-scale wrinkling of the flame occurs before the flame tip pinches off, leading to an overall increase in the flame surface and amplitude of the fluctuating global heat release rate.

1. Introduction

Gas turbines burning hydrogen can potentially help deliver large-scale zero carbon power generation and facilitate rapid decarbonisation over the short to medium term. They can also play a crucial role in increasing the penetration of renewable energy sources via power to hydrogen to power cycles where excess electricity is used to produce hydrogen. This marks a shift away from their traditional role of providing a constant base load to dynamic operation. Using hydrogen as primary fuel in lean premixed combustion regimes poses certain challenges such as flashback, autoignition, and thermoacoustic instabilities [1–3]. In this paper we focus on the latter.

Thermoacoustic instabilities occur when fluctuations in the heat release rate respond to fluctuations in the flow that are coupled to combustor acoustics in a feedback loop and are a major challenge in the development of gas turbines. Low-order acoustic network models, which are used to predict thermoacoustic instabilities, require information about the relationship between the acoustically driven velocity fluctuations and the fluctuations in the heat release rate as the flame acts as a source of acoustic energy. A standard approach is to construct a Flame Transfer Function (FTF) which aims to capture how the fluctuations of the global heat release rate (HRR) respond to fluctuations in the flow velocity over a range of frequencies [4]. It has been known for a long time that the time delay between the pressure and HRR fluctuations is a key parameter that often determines the stability of a combustor [5]. Normally FTFs are empirically derived and therefore obtained from experiments as they encode burner specific information [6–9] but they can also be extracted from numerical simulations [10], or theoretically derived [11–14].

The FTF is expected to behave as a low-pass filter with a cut-off frequency determined by the flame length and an approximately linear development of the phase for a constant convective time-delay [11,15]. A number of studies have reported various departures from the low-pass behaviour in the form of modulations in the gain and phase [16–20]. By changing the axial location of a swirler Komarek and Polifke [16] observed that the gain exhibited modulations at different frequencies. Similar

* Corresponding author.
E-mail address: eirik.asoy@ntnu.no (E. Æsøy).

https://doi.org/10.1016/j.combustflame.2021.111813

modulations were also produced by changing the location of fuel injection in a technically premixed configuration [21]. In separate but contemporaneous studies, Palies et al. [17] also observed modulations in the gain in swirling premixed flames leading to the hypothesis that the modulations may originate from fluctuations in the swirl number due to convective-acoustic interactions between vorticity waves shed from the swirler and acoustic waves [22,23].

Further insight into the origin of the modulations was recently presented in a set of papers by Gatti et al. [18,24]. They demonstrated that specific changes to the burner geometry could generate a large dip in the gain which coincided with the suppression of vortical structures (measured by PIV) at frequencies where the dips occurred showing that the modulations may be driven by disturbances produced by the upstream cold flow. However, it was also suggested that both a swirler and a center rod were still important components in the generation of modulations in the gain.

Æsøy et al. [15] also observed the presence of modulations in hydrogen/methane and pure hydrogen flames. However, there were two important differences. Firstly, hydrogen enriched and pure hydrogen flames result in very short compact flames which significantly increases the cut-off frequency of the FTF compared with methane flames increasing the range over which modulations could form and secondly, the flames did not employ swirl. The modulations were shown to emanate from convective-acoustic interference from vortex shedding upstream but more importantly showed that swirl itself was not an important mechanism but rather that geometries that produce small but sufficiently phased convective disturbances lead to convective-acoustic interference. In a continuing study [25] the cold flow was investigated in detail and it was shown that similar modulations appeared in a hydrodynamic transfer function relating the acoustic and total velocity oscillations measured at the burner exit. The study showed that the modulations of the total velocity were proportional to the modulations of the HRR indicating that the effect is hydrodynamic and that the response is linear.

In this paper, we investigate the effect of flow disturbances generated upstream by three different geometries; a set of small diameter cylinders, a streamlined body, and a swirler. Their upstream location is varied to adjust the relative time-delay between the acoustic forcing and when the flow disturbances reach the flame base and elucidate how they govern acoustic-convective interference. We furthermore demonstrate how the acoustic forcing and flow disturbances can be tuned to modify the gain and phase of FTFs without significant changes to the stabilisation or the mean structure of the flame. The tuning approach is based on the concept of distributed time lags (see [15,26]) which are used to identify the optimal location for the upstream geometry needed to produce convective disturbances that result in large amplitude modulations in the gain and phase over a narrow band frequency range in the FTF. We also present high-speed imaging of OH*-chemiluminescence and Planar Laser Induced Fluoresecence (OH-PLIF) to better understand the link between the modulations and the flame dynamics.

The paper layout is as follows: Section 2 describes the experimental set-up, measurement and analysis methods used, in Section 3, measurements of the FTF for three different upstream geometries (streamlined bodies, a swirler and circular cylinders) are presented. In addition, a method to tailor the acoustic/convective interference and control the FTF gain and phase is presented and analysed. In Section 4 we consider how the flame responds to convective-acoustic interference using flame-front tracking methods to link the acoustic/convective interference to the flame sheet kinematics. Section 5 summarizes the main conclusions.

2. Experimental set-up and methods

2.1. The burner set-up

A schematic of the burner geometry is shown in Fig. 1 and is similar to the set-up used in [15]. The cylindrical quartz combustion chamber had a diameter of 44mm and a length of 50mm which was sufficiently short to avoid self-excited instabilities but long enough to enclose the flame. The bluff body had a diameter $d_\mathrm{b} = 13$mm with a 45° inclination angle and was mounted to a rod of diameter $d_\mathrm{r} = 5$mm.

A Cartesian coordinate system (x, y) in the streamwise and radial directions respectively is used with the origin placed at the center of the bluff body as shown in Fig. 1 b). Polar coordinates (r, θ), when used, denote the location of the relative blockage locations on each of the geometries. Three different geometric shapes were placed upstream at $L_g = 30$mm and 50mm from the bluff body as shown in Fig. 1 a). They include a set of $d_g = 10$mm long and 2.5mm wide streamlined bodies with aspect ratio 4, circular cylinders of diameter $d_g = 5$mm, and a six-vaned swirler with a chord length of $d_g = 11$mm used previously [20,27]. The subscript d_g denotes the characteristic length of the upstream geometry (chord length, diameter of the cylinders and swirler vane length).

Each produces flow disturbances (vortex/wake shedding) of varying degree locked into the forcing frequency at Strouhal number, $\mathrm{St}_{\mathrm{d}_g} = f d_g/\bar{u}_p$, that constructively or destructively interferes with the acoustic fluctuations at the burner exit. Premixed flames using different blends of hydrogen, methane and air were investigated at a constant equivalence ratio $\Phi = 0.7$. The fraction of hydrogen by power is $\mathrm{P_H} = 0.4$ for the non-swirled and $\mathrm{P_H} = 0.2$ for the swirled cases to avoid flashback. This corresponds to volume fractions of $\mathrm{V_H} = 0.67$ and $\mathrm{V_H} = 0.43$, respectively. $\mathrm{P_H} = \frac{\mathrm{P_{H_2}}}{\mathrm{P_{H_2}+P_{CH_4}}}$ and $\mathrm{V_H} = \frac{\mathrm{V_{H_2}}}{\mathrm{V_{H_2}+V_{CH_4}}}$, where $\mathrm{P_{H_2}}$ and $\mathrm{P_{CH_4}}$ are the thermal powers from hydrogen and methane, and $\mathrm{V_{H_2}}$ and $\mathrm{V_{CH_4}}$ are the volume flow rates of hydrogen and methane. Fuel and air flows were controlled by individual Alicat mass flow controllers (MFCs) which were combined together approximately 1m upstream before entering the plenum for premixing.

Several exit velocities $\bar{u} = [10, 20, 30, 40]$ m/s measured at the bluff body were investigated. This corresponds to inlet velocities $\bar{u}_\mathrm{p} = [5.7, 11.4, 17.1, 22.9]$ m/s which are the relevant velocity scale for the vortex shedding from upstream geometries. Acoustic forcing was provided by two Monacor KU-516 horn drivers mounted in the plenum in combination with an Aim-TTi TGA1244 signal generator and a QTX Sound PRO1000 power amplifier. The operating conditions are summarized for all cases in Table 1.

2.2. Pressure measurements

The reference acoustic velocity fluctuations $\hat{u}(x)$, were obtained at the burner dump plane using the multiple microphone method (MMM) [28]. The acoustic pressure and velocity fluctuations are given by $p'(x,t) = \mathrm{Re}\{\hat{p}(x)e^{\mathrm{j}\omega t}\}$ and $u'(x,t) = \mathrm{Re}\{\hat{u}(x)e^{\mathrm{j}\omega t}\}$ respectively. Here, $\omega = 2\pi f$ is the angular frequency, and $\hat{p}(x)$ and $\hat{u}(x)$ are given by:

$$\hat{p}(x) = A^+ \exp\left(-\mathrm{j}k_x^+ x\right) + A^- \exp\left(\mathrm{j}k_x^- x\right), \tag{1a}$$

$$\hat{u}(x) = \frac{1}{\bar{\rho}\bar{c}}\left(A^+ \exp\left(-\mathrm{j}k_x^+ x\right) - A^- \exp\left(\mathrm{j}k_x^- x\right)\right). \tag{1b}$$

In Eq. (1) the complex valued A^+ and A^- are the amplitude and phase (Riemann invariants) of upstream and downstream propagating 1D acoustic waves. The quantities $\bar{\rho}$, $\bar{c}$ and $k_x^\pm = k_x/(1 \pm \bar{u}/\bar{c})$

Table 1
Summary of operating conditions in terms of the upstream geometry, distance from the upstream geometry to the dump plane L_g, hydrogen power fraction P_H, hydrogen volume fraction V_H, equivalence ratio Φ, thermal power P, and bulk velocities $\bar{u}_p$ and $\bar{u}$ inside the pipe and at the dump plane respectively..

Geometry	L_g [mm]	P_H	V_H	Φ	P [kW]	$\bar{u}_p$ [m/s]	$\bar{u}$ [m/s]
Streamlined	50	0.4	0.67	0.7	3.5	5.7	10
Streamlined	50	0.4	0.67	0.7	7.0	11.4	20
Streamlined	50	0.4	0.67	0.7	10.5	17.1	30
Streamlined	50	0.4	0.67	0.7	14.0	22.9	40
Cylinder	50	0.4	0.67	0.7	3.5	5.7	10
Cylinder	50	0.4	0.67	0.7	7.0	11.4	20
Cylinder	50	0.4	0.67	0.7	10.5	17.1	30
Cylinder	50	0.4	0.67	0.7	14.0	22.9	40
Swirler	50	0.2	0.43	0.7	3.4	5.7	10
Swirler	50	0.2	0.43	0.7	6.9	11.4	20
Swirler	50	0.2	0.43	0.7	10.3	17.1	30
Swirler	50	0.2	0.43	0.7	13.8	22.9	40
Cylinder	30	0.4	0.67	0.7	3.5	5.7	10
Cylinder	30	0.4	0.67	0.7	7.0	11.4	20
Cylinder	30	0.4	0.67	0.7	10.5	17.1	30
Cylinder	30	0.4	0.67	0.7	14.0	22.9	40
Swirler	30	0.2	0.43	0.7	3.4	5.7	10
Swirler	30	0.2	0.43	0.7	6.9	11.4	20
Swirler	30	0.2	0.43	0.7	10.3	17.1	30
Swirler	30	0.2	0.43	0.7	13.8	22.9	40

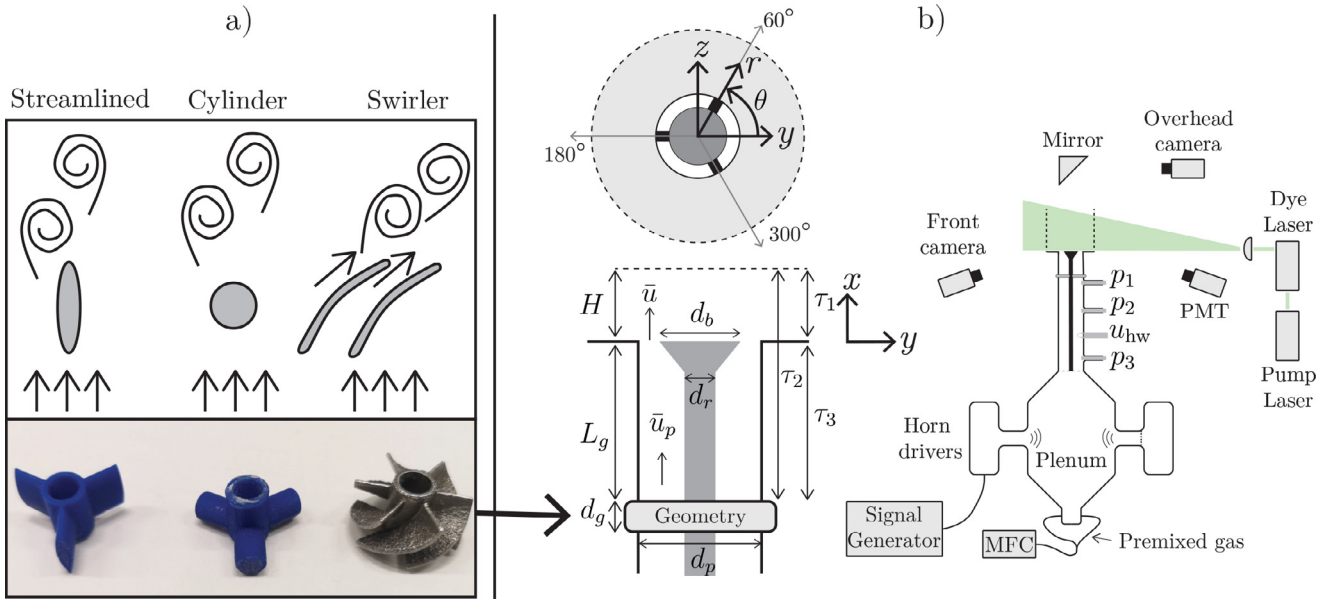

Fig. 1. Schematic of the experimental set-up and different upstream geometries investigated. a) shows images of the three geometries investigated and a schematic of the vortex shedding behind each of these. b) shows a schematic of the experimental set-up, including the injector pipe geometry with the bluff body and the location of the upstream geometries where the important time delays are indicated, a top view showing their angular location, and a front view showing the diagnostics and instrumentation.

are the density, the speed of sound and the stream-wise wave number respectively. Note that $k_x^{\pm}$ is modified by the mean flow, where $k_x = 2\pi f/c$. Eq. (1) is valid inside the pipe and the influence of the upstream geometries are negligible, which was verified experimentally. The influence of the bluff body was modeled as an acoustically compact area jump. The dynamic pressure was measured using Kulite XCS-093-0.35D pressure transducers at three locations denoted p_i for $i = 1, 2, 3$ shown in Fig. 1 b). The signals were sampled at a rate of 51.2kHz for 10s and digitized using a 24-bit NI-9234 DAQ. Spectral analysis was used to obtain $\hat{p}(x_i)$ and $A^{\pm}$ by solving for the two unknowns in Eq. (1a).

The measured values of $\hat{p}_i$, in Eq. (1a), were evaluated by:

$$\hat{p}_i = \hat{p}(x_i) = \frac{\mathrm{PSD}\left(p'_{\mathrm{ref}}, p'_i\right)}{\sqrt{\mathrm{PSD}\left(p'_{\mathrm{ref}}, p'_{\mathrm{ref}}\right)}}, \tag{2}$$

where $\mathrm{PSD}\left(p'_{\mathrm{ref}}, p'_i\right)$ is the cross power spectra between the reference signal p'_{ref} from the signal generator and the measured pressure fluctuations p'_i. Each spectrum was obtained using the Welch method by averaging 50% overlapping segments of the signal multiplied by a Hanning window.

2.3. FTF measurements

FTFs were measured at a constant forcing level $|\hat{u}|/\bar{u} = 0.05$ at the dump plane over the frequency range $f = 25 - 2000$Hz. Normalised fluctuations of the heat release rate were obtained using a Hamamatsu H11902-113 photomultiplier tube (PMT) equipped with a UV band pass filter (310 ± (10)nm). It has been well established that in premixed flames the measured intensity is approximately proportional to the global HRR $Q(t) = \bar{Q} + Q'(t)$ [11,29–32].

FTFs were then calculated using [7,11]:

$$\mathrm{FTF}(\omega) = \frac{\hat{Q}/\bar{Q}}{\hat{u}/\bar{u}} = G\exp\left(j\Theta\right). \tag{3}$$

The acoustic velocity $\hat{u}$ was obtained from Eq. (1b), while the complex valued HRR $\hat{Q}$, was obtained using Eq. (2) but substituting for various HRR terms. The FTF was decomposed into a gain G and a phase Θ, which describe the relative magnitude and phase between the two quantities, $\hat{Q}$ and $\hat{u}$ respectively.

2.4. High-speed imaging: Chemiluminescence and PLIF

To characterize the flame dynamics high speed imaging of OH*-chemiluminescence from both the side ($x-y$ plane) and top ($y-z$ plane) views of the flame were obtained. OH-PLIF was also acquired in the $x-y$ plane for selected frequencies. Two high speed cameras each equipped with LaVision Intensified Relay Optics (IRO) unit, a Cerco 2178 UV lens (100F/2.8), and a notch filter $310\pm(10)$nm were used. Top views of the flame were obtained using a cooled mirror mounted at 45° approximately 1.5m above the flame. The spatial resolution of the side and top images is 11.7pixel/mm and 8.8pixel/mm.

The OH-PLIF system was comprised of a 100W green (532nm wavelength) Edgewave laser used to pump a Sirah Credo-Dye-N laser beam collimated to an approximately 1mm thick laser sheet in the $x-y$ plane. The output wavelength of the dye laser was tuned to the OH absorption peak near 281nm and the power output was approximately 3W at 10kHz. A gate time of 80nm was used to ensure that only the OH radicals excited by the laser pulse were captured. To extract the flame surface the following post-processing steps were followed: 1) a laser sheet intensity correction, 2) Gaussian smoothing, and 3) a Canny edge detection algorithm [33], similar to the approach used in [30,34,35]. The edge detection provides a binary image where $s=1$ for the pixels where the flame front is located providing a set of flame surface coordinates (x_s, y_s).

2.5. FTF described by the DTL model

To identify general trends and scalings of the flame response related to the cut-off frequency, phase development, as well as low frequency gain and phase modulations, measurements were fitted to a distributed time lag (DTL) model [26]. The general form of the model is given by:

$$\mathrm{DTL_T} = \mathrm{DTL_1} + \mathrm{DTL_2} = \left(E_1^+ + E_1^-\right) + \left(E_2^+ + E_2^-\right), \tag{4a}$$

$$E_i^{\pm} = \frac{g_i}{2}\exp\left(-\frac{1}{2}(\omega\pm\beta_i)^2\sigma_i^2 - j\omega\tau_i\right), \tag{4b}$$

where Eqs. (4a) and (4b) are a linear combination of two normally distributed time lags in the frequency domain, $\mathrm{DTL_1}$ and $\mathrm{DTL_2}$, that describe the global HRR response to velocity fluctuations. The modulation frequency β_i corresponds to the preferred frequency where the maximum response of each distribution occurs and g_i, σ_i^2, and τ_i are the gain, variance, and mean time delay respectively. The model and fitting procedure were described in detail in [15].

To illustrate the physics of the problem being modeled, we show a sketch of the relevant time-scales and dimensions in Fig. 1 b). The time lags that are represented within the DTL model parameters are solved relative to the centre of heat release $H = \max_x\left(\bar{q}_{yz}\right)$ obtained from the mean flame image. As shown in Fig. 1 b), $\tau_1 \approx H/\bar{u}$ and is the time taken for acoustic velocity fluctuations to travel from the dump plane to H whereas $\tau_2 \approx H/\bar{u} + L_g/\bar{u}_p$ is the time taken by a vortex shed from the upstream geometry (locked into the forcing frequency) to reach H. At a fixed operating condition, the interaction between $\mathrm{DTL_1}$ and $\mathrm{DTL_2}$ is therefore controlled by the relative time-delay $\tau_3 = \tau_2 - \tau_1$ which only depends on the distance L_g and $\bar{u}_p$. Due to the increase of $\bar{u}_p$ over the contraction of the bluff body a correction is added to L_g which is reduced by 1.55mm when computing τ_3.

To characterise the interference between these time delays it is convenient to rewrite Eq. (4) as:

$$\mathrm{DTL_T} = \mathrm{DTL_1}\left(1 + \frac{|\mathrm{DTL_2}|}{|\mathrm{DTL_1}|}\exp\left(j2\pi f\tau_3\right)\right), \tag{5a}$$

$$f\tau_3 \approx \frac{fL_g}{\bar{u}_p}, \tag{5b}$$

where $f\tau_3$ is the non-dimensional time-delay which determines the phase between the two sources. Under the condition that $|\mathrm{DTL_2}| < |\mathrm{DTL_1}|$, the second term in Eq. (5a), can be considered a modulation term. Whenever $f\tau_3$ is integer valued, i.e. $f\tau_3 = N$ where $N \in \mathbb{N}$, the two contributions are in phase, resulting in peaks in the gain of the FTF. Therefore the wavelength of the modulations in the gain is inversely proportional to $1/\tau_3$. Similarly, a minimum in the gain occurs when $f\tau_3 = N \pm 1/2$. When $f\tau_3 = N \pm 1/4$, the two contributions are 90° out-of-phase, resulting in a relatively large shift in the phase but a comparatively small modulation in the gain. We show how to use these features to tailor the gain and phase of the FTF in the next section.

3. Tailoring the Flame Transfer Function

3.1. FTFs for different upstream geometries

A set of FTFs were measured with each set of geometries placed at $L_g = 30$mm and 50mm upstream of the dump plane for a range of $\bar{u}$. These are shown in Fig. 2 a), b), and c) for the streamlined bodies, cylinders, and the swirler respectively. The corresponding mean flame shapes are also plotted in Fig. 3 for selected operating conditions. Particular care was taken to align the image plane with one of the cylinders and streamlined goemetries shown in Fig. 1 to capture their effect on mean flame shape. Panel d) shows the presence of a small asymmetry of the mean flame shape which exhibit weaker modulations in the FTF gain whereas the strongest modulations occur in flames a), b), f) and g) which appear approximately axisymmetric. As small deviations in axisymmetry are often observed in flames, this serves to demonstrate how the mean flame shape is not a reliable indicator of the presence of non-uniformities in the base flow that may affect the transfer function.

Figure 2 shows that the cut-off frequencies collapse when scaling with a Strouhal number based on the centre of heat release H, $\mathrm{St}_H = fH/\bar{u}$. We can also express St_H as an equivalent non-dimensional time-delay: $\mathrm{St}_H = f\tau_1$. Figure 2 shows that streamlined body and cylinders show good collapse of the cut-off frequency whereas the swirler shows a reasonable but less effective degree of collapse. This is due to the reference velocity scale being ill defined as $\bar{u}$ does not take the tangential velocity component into account.

When the upstream geometries are placed at $L_g = 50$mm, weak modulations in the gain are observed for the streamlined bodies, become more pronounced with the cylinders, and are strongest in swirling flames [16,17,20,24]. The wavelengths and relative phase of the modulations do not scale with St_H exemplified by the swirler case in Fig. 2 c). This demonstrates that an additional non-dimensional group is needed to scale both the cut-off frequency behaviour and the modulations of the FTF.

Figure 4 plots the modulations in the gain in the low-frequency range for the cyclinder and swirler geometries at $L_g = 30$mm and 50mm scaled by $fL_g/\bar{u}_p$ and $fd_g/\bar{u}_p$ for comparison. The figure shows that positioning the upstream geometries closer to the burner exit increases the amplitude of the modulations (the disturbances have less time to decay) and that scaling by L_g best aligns

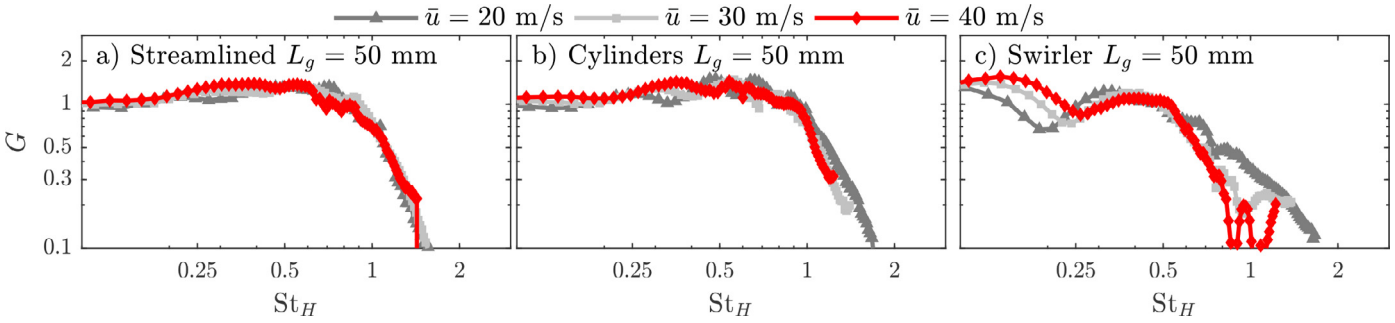

Fig. 2. Gain G of measured FTFs for the different upstream geometries (streamlined body, cylinder, and swirler) at different velocities. The gain cut-off is collapsed well for the cases with streamlined bodies and cylinders, and reasonably well for the cases with the swirler by scaling the FTFs by the time delay $\mathrm{St}_H \approx fH/\bar{u} \approx f\tau_1$.

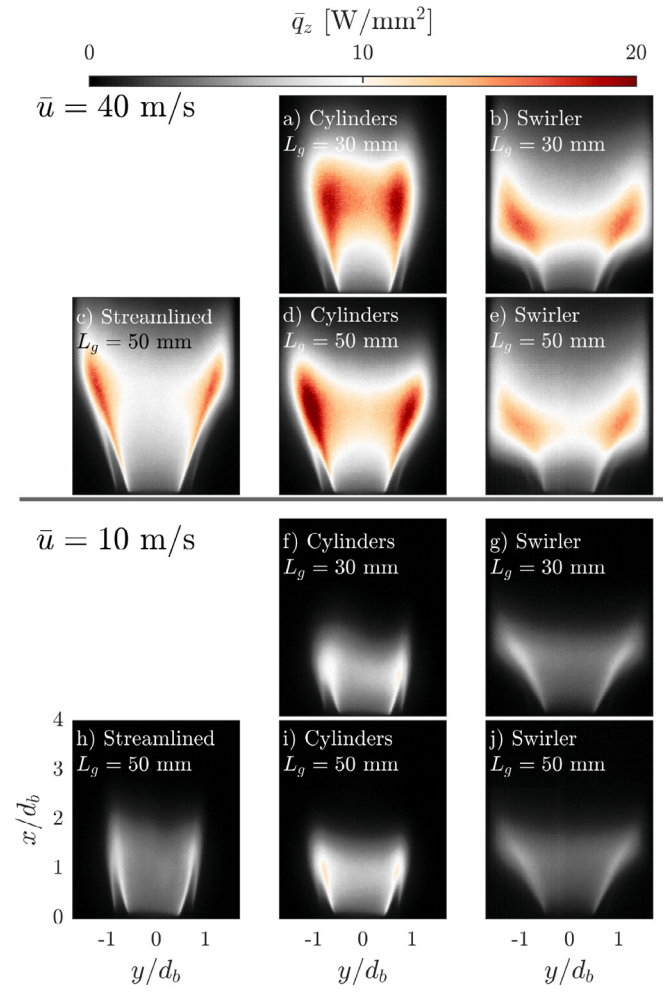

Fig. 3. Time-averaged flame shapes viewed from the side $\bar{q}_z$. The top set of images are taken at $\bar{u} = 40$m/s and the bottom set at $\bar{u} = 10$m/s. The different position L_g and type of geometry are annotated in each panel.

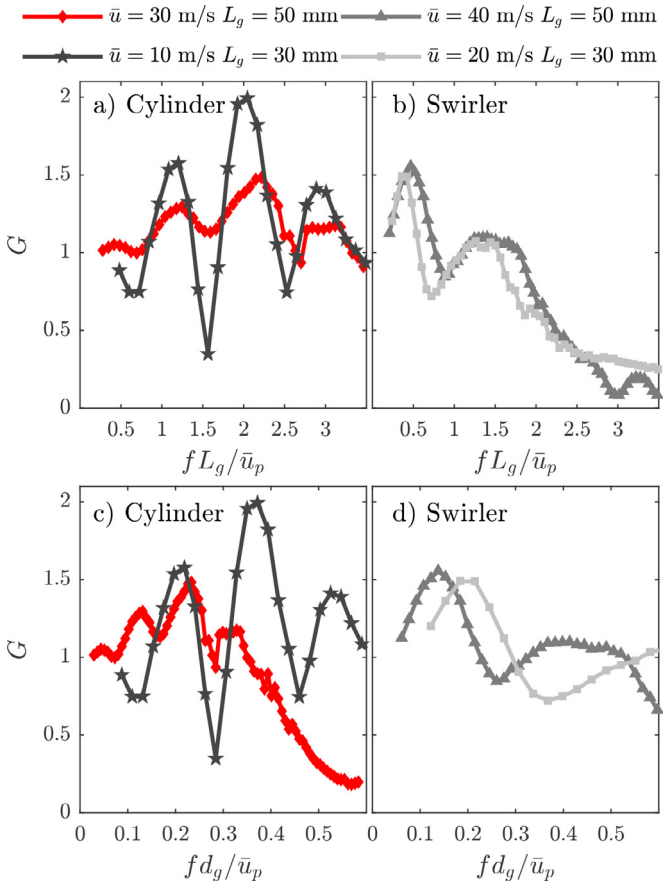

Fig. 4. Scaling of the gain modulations of the FTFs. In a) and b) the acoustic/convective interference is collapsed by scaling the frequency by $fL_g/\bar{u}_p$, aligning the modulations. In c) and d) the acoustic/convective interference is collapsed by scaling the frequency by $fd_g/\bar{u}_p$, showing that the band of the interference centers on a natural shedding frequency close to $fd_g/\bar{u}_p \approx$ [0.2 to 0.4].

the wavelengths of the modulations. This shows that the wavelength and hence characteristic time-scale of the modulations are governed by τ_3 but the physical origin of the modulations is the vortex shedding which scales with St_{d_g}, where large modulations appear close to $\mathrm{St}_{d_g} \approx$ [0.2 to 0.3] consistent with scaling of the Kármán vortex street [36]. Again, in the case of the swirling flames the azimuthal component will alter the velocity scale and time-delay associated with convective disturbances downstream of the swirler, which has been shown to propagate as inertial waves at a different velocity than the axial bulk flow velocity [37].

3.2. Generating strong modulations in the FTF gain

We now demonstrate how strong modulations can be produced by the upstream geometry. Figure 5 shows the FTF of the cylinders when placed upstream at $L_g = 30$mm for $\bar{u} = 10$m/s, corresponding to the black line with stars in Fig. 4, which results in strong low-frequency modulations. The corresponding DTL model of the FTF is shown by the solid line. At non-dimensional time delays $f\tau_3 \approx 1.5$ and 2.5 the gain is suppressed to minimum values whereas integer values $f\tau_3 \approx 1$ and 2 show regions of large amplification. These changes to the gain are also accompanied by abrupt changes in the phase. The underlying physical mecha-

Table 2
Fitted constants of the DTL model and comparison with physical time delays shown in Fig. 1b) for $\bar{u} = 10$m/s at $L_g = 50$mm and 30mm.

L_g [mm]	g_1 [-]	$1/\sigma_1$ [kHz]	β_1 [kHz]	τ_1 [ms]	g_2 [-]	$1/\sigma_2$ [kHz]	β_2 [kHz]	τ_2 [ms]	$\mathrm{St}_{d_g} = \beta_2 d_g/\bar{u}_p$ [-]	$\tau_1\bar{u}/H$ [-]	$\tau_3\bar{u}_p/L_g$ [-]
50	1.49	0.54	0.35	1.3	0.18	0.15	0.29	8.9	0.25	0.94	0.92
30	1.22	0.51	0.37	1.13	0.84	0.14	0.37	5.8	0.32	1.01	0.98

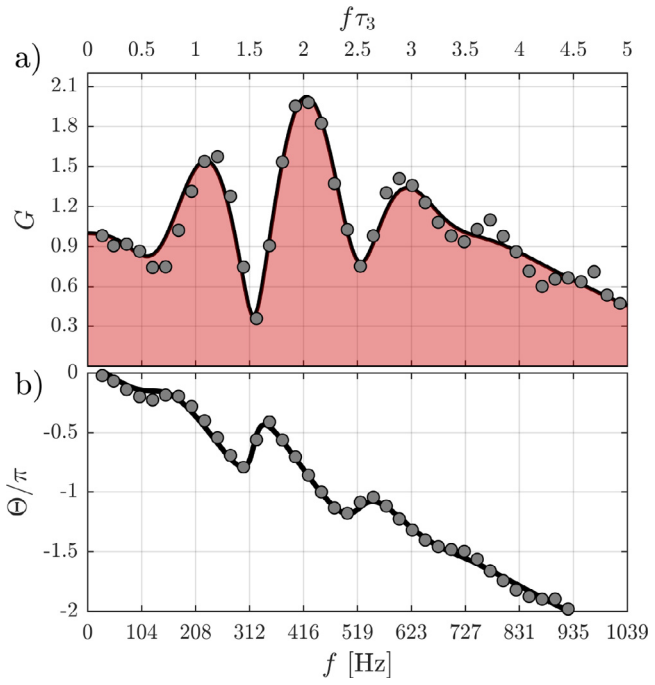

Fig. 5. Gain a) and phase b) of the FTF with strong modulations with the cylinder placed at $L_g = 30$mm at $\bar{u} = 10$m/s. (∘) and (—) show the measurements and fitted model $\mathrm{DTL_T}$ respectively, which are in excellent agreement.

nisms appear in the model constants summarized for $L_g = 30$mm and 50mm in Tab. 2. All the model constants are very similar for both L_g except for g_2 and τ_2. This shows that the acoustic response of the flame τ_1 is not strongly dependent on L_g. The main effect of moving L_g is the adjustment of the time delay τ_2 which, in turn, causes a large increase in the magnitude of the gain modulations g_2 from 0.18 to 0.85. This drastic increase in g_2 is due to the decay of the vortex shedding which has been shown to decrease exponentially for $L_g/d_g > 5$ in cylinder wakes [38]. In other words, if L_g is chosen sufficiently short ($L_g/d_g < 7$) increasing or decreasing L_g affects the combined time-delay τ_3 which can be tuned to suppress the gain over a given range of frequencies.

We can use the DTL model to identify the modulation frequency β_2 and the non-dimensional vortex shedding frequency from the cylinders $\mathrm{St}_{d_g} = \beta_2 d_g/\bar{u}_p$. We find $\mathrm{St}_{d_g} = 0.32$ and 0.25, which are in good agreement with the optimal range of non-dimensional shedding frequencies of flow around a cylinder over a wide range of Reynolds numbers [36]. From the DTL model we find a range of $\mathrm{St}_{d_g}(1 \pm 3\beta_2\sigma_2)$ which exhibits a band pass filter structure centered on $f = \beta_2$ where the maximum modulation of the amplitudes in the gain and phase occur. This envelope is plotted in red in Fig. 7 and can be used to effect large changes in the gain and phase response over a specific frequency range as discussed in the next sections. This envelope results from lock-on of the non-dimensional optimal vortex shedding frequency to the acoustic forcing frequency [39].

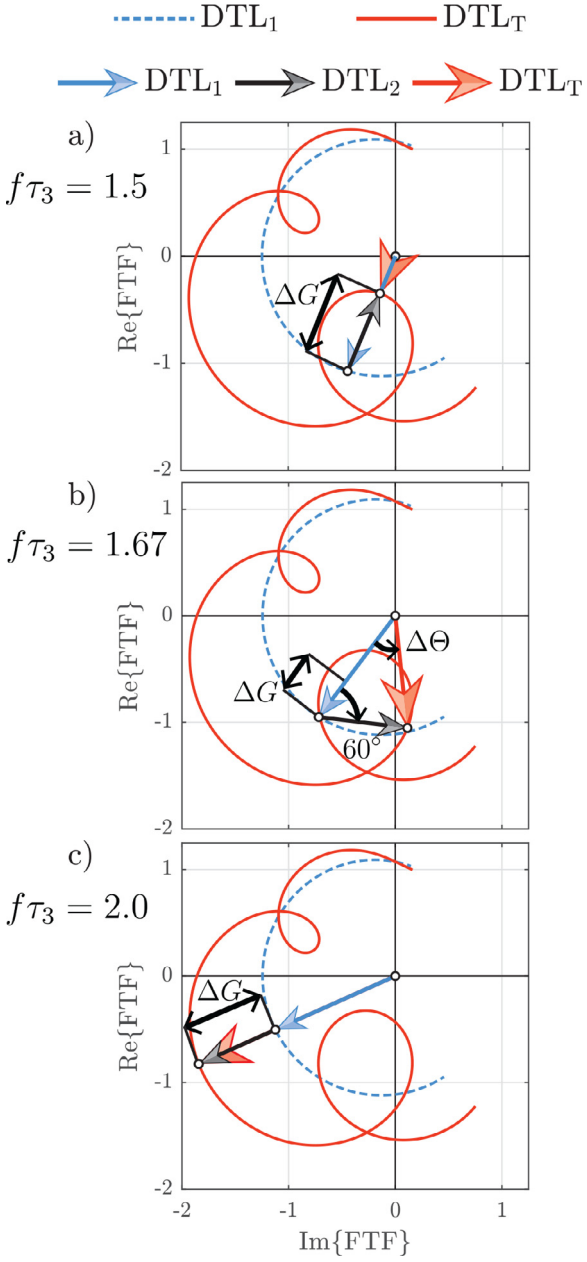

Fig. 6. The FTF shown in the complex plane as phasors for $L_g = 30$mm in the range $f\tau_3 = [1 \text{ to } 3.5]$, corresponding to large gain and phase modulations. The arrows show the two vectors $\mathrm{DTL_1}$, $\mathrm{DTL_2}$ and their sum $\mathrm{DTL_T}$ at a) destructive gain interference at $f\tau_3 = 1.5$, b) large phase modulation at $f\tau_3 = 1.67$, and c) constructive gain interference at $f\tau_3 = 2.0$. The second source (vortex shedding) of convective perturbations, described by $\mathrm{DTL_2}$, modulates the gain and phase of $\mathrm{DTL_1}$.

3.3. Controlling the gain and phase modulations

How the convective and acoustic sources interfere can be illustrated using the phasor diagrams plotted in Fig. 6 for $L_g = 30$mm. Equation (5a) expresses the total response of the FTF as an interaction between $\mathrm{DTL_1}$ and $\mathrm{DTL_2}$ where $f\tau_3$ determines their relative

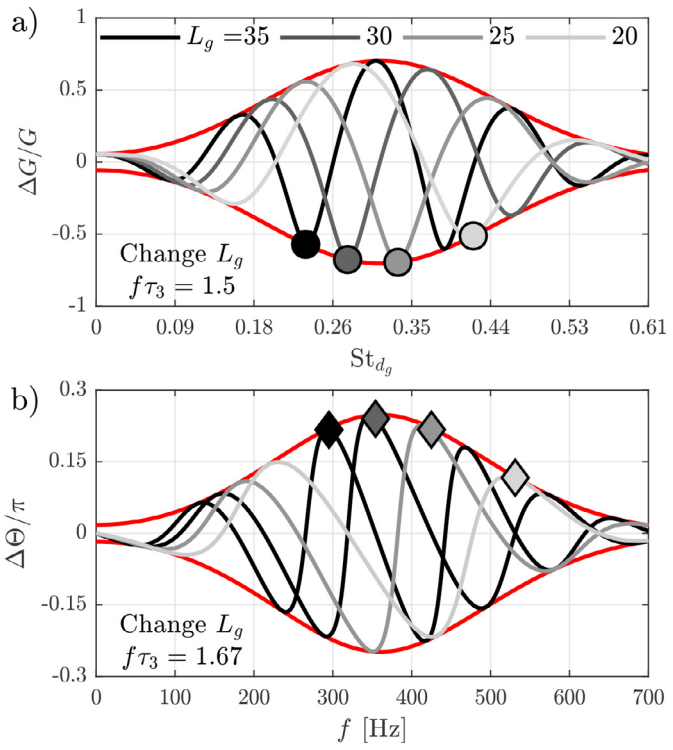

Fig. 7. Tuning of a) the gain $\Delta G/G$ and b) the phase $\Delta\Theta/\pi$ by controlling the cylinder location L_g. The line (—) shows the envelope of potential modulations and the gray lines show the modulations at the different cylinder positions where $L_g = 35$mm (—), 30mm (—), 25mm (—), and 20mm (—). Markers are added at $f\tau_3 = 1.5$(●) in a) and at $f\tau_3 = 1.67$(◆) in b) to show how matching $f\tau_3$ leads to large modulations at frequencies of interest. (For interpretation of the references to colour in their figure legend, the reader is referred to the web version of this article.)

phase, and thus the superposition between the acoustic and convective sources. The arrows indicate the direction of the vectors DTL_1, DTL_2, and their sum DTL_T in the complex plane of the FTF. The length, $|\mathrm{DTL}_\mathrm{T}| = G$, and the angle, $\angle(\mathrm{DTL}_\mathrm{T}) = \Theta$, correspond to the gain and phase respectively.

When $f\tau_3 = 1.5$ and 2.0, as shown in a) and c), the vectors are parallel leading to a minimum and maximum in the gain respectively. Parallel vectors lead to a negligible shift in Θ but a large shift in G denoted by ΔG in the figure. When $f\tau_3 = 1.5$ the two sources are a half-cycle out-of-phase resulting in a reduction in ΔG, whereas when $f\tau_3 = 2.0$ the two sources are in phase and ΔG increases (by roughly a factor of 4). When the two vectors approach orthogonality, a large shift of the phase $\Delta\Theta$ occurs with a relatively small ΔG. Although not quite orthogonal, this is observed by the large shift in the phase in Fig. 6 b). This also corresponds to the phase jump observed in Fig. 5 for $f\tau_3 = 1.67$.

The expression in Eq. (5a) provides an explicit way to predict and control the frequencies of constructive and destructive interference as a function of $f\tau_3$. We now have the parameters/scalings needed to control the gain and phase of the modulations. Through careful selection of the upstream geometry and its location L_g, the gain and phase of the FTF can be modified over a range of selected frequencies and passively suppress self-excited instabilities.

To illustrate the procedure we use the cylinders as the upstream geometry to take advantage of the Strouhal number scaling. To modify the gain or phase at a given operating condition (a fixed flowrate) requires the following procedure:

1. Identify the target frequency or centre of the frequency range where modifications to the gain or phase are required. For example, a resonant mode that requires suppression. Select the diameter of the cylinders, d_g, so that the non-dimensional shedding frequency lies in the range $\mathrm{St}_{d_g} = [0.2 \text{ to } 0.4]$, where f is set to the target acoustic frequency. Matching the non-dimensional shedding frequency St_{d_g} with the acoustic frequency is required to ensure lock-on.
2. Next, the cylinder location L_g should be chosen to provide the desired range of non-dimensional time delays, $f\tau_3$, which controls the level of interference between the convective and acoustic disturbances. This can be chosen to either modify the gain or the phase over a range of frequencies centred on the target frequency. To achieve a large suppression in the gain, $f\tau_3 = N \pm 1/2$ should be matched, and for a large shift of the phase, $f\tau_3 \approx 0.33 + N$ or $f\tau_3 \approx 0.67 + N$ should be matched. The cylinder location must also be sufficiently close to the flame base such that g_1 and g_2 are in the same order of magnitude. If the cylinders are too far upstream, the coherent structures will decay limiting their effect on the flame response.

These two steps can be thought of as firstly, exploiting the Strouhal number scaling to generate optimal convective-acoustic disturbances over a targeted frequency range and secondly, using their relative time-delay to amplify or damp the gain or phase as required. The method is illustrated in Fig. 7 which shows the effect of different cylinder positions L_g on the relative change in the gain $\Delta G/G$ and phase $\Delta\Theta/\pi$. Note that a) and b) show the non-dimensional and equivalent dimensional frequencies respectively to ease interpretation.

Figure 7 a) shows how the gain can be tuned by adjusting L_g. The line for $L_g = 30$mm corresponds to DTL_T fitted to the measurements. Lines for the other values of L_g were obtained using the DTL model by varying the time-delay τ_2. The other model parameters are all approximately constant except for the gain g_2 which changes with L_g. The large markers denote when the non-dimensional time-delay $f\tau_3 = 1.5$, which corresponds to the largest reduction in the gain for each L_g (see Fig. 5 when $L_g = 30$ mm). As L_g changes, the frequencies where minimum (and maximum) values of $\Delta G/G$ occur are shifted.

Figure 7 b) shows how the phase can also be tuned by adjusting L_g. The large markers denote when the non-dimensional time-delay $f\tau_3 = 1.67$, which corresponds to the largest positive change in the the phase $\Delta\Theta$. As is the case for the gain, the frequencies where the maximum $\Delta\Theta$ occur shift depending on L_g. At these frequencies large modulations in the gain or shifts in the phase can be achieved and shows how time delays can be used to tailor the gain and phase at specific frequencies.

However, by decreasing the gain at a selected range of frequencies we also increase the gain at other frequencies. This might be a limitation of the method that leads to mode switching instead of suppression of the instability. Hence, testing the strategy on a configuration undergoing self excited oscillations remains a task for future studies.

4. Flame dynamics and analysis of interference

4.1. Phase averaged heat release rate

We now investigate the dynamics associated with the global interference. The global and spatial signals of the HRR Q and q were obtained in the range $f\tau_3 = [1.1 \text{ to } 3.6]$ which correspond to the large gain modulations presented in Fig. 5.

Figure 8 plots the rms fluctuations and the magnitude of the coherent fluctuations obtained from the Fourier modes (see Appendix A) $\hat{q}_x$ and $\hat{q}_z$ in a) and b) respectively. Both top and side views are presented. The rms fluctuations are similar for all frequencies despite the large gain increase from $G = 0.4$ to 2.0 be-

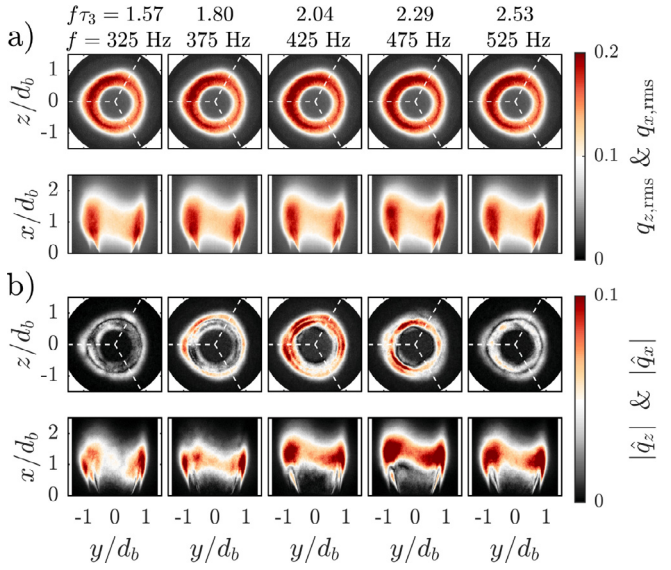

Fig. 8. Magnitude of HRR fluctuations in the range $f\tau_3 = [1.57 \text{ to } 2.53]$, corresponding to large gain and phase modulations in the FTF. a) shows rms fluctuations $q_{x,\mathrm{rms}}$ (top view) and $q_{z,\mathrm{rms}}$ (side view). b) shows magnitude of the Fourier modes $|\hat{q}_x|$ and $|\hat{q}_z|$. All images are normalized by the maximum HRR obtained from the mean flame image $\bar{q}_{z,\max}$ and $\bar{q}_{x,\max}$.

tween $f\tau_3 = 1.57$ to $f\tau_3 = 2.04$ and then decrease from $G = 2.0$ to 0.7 between $f\tau_3 = 2.04$ to $f\tau_3 = 2.53$.

However, the Fourier modes in Fig. 8 b) shows a distinct response that follows the gain modulations in both top and side views. At the gain minimum, $f\tau_3 = 1.57$ the top view shows $\hat{q}_z$ reaches a minimum and increases to peak values at $f\tau_3 = 2.04$ which corresponds to the maximum gain in Fig. 5.

To understand the effect of the modulations on the flame response in more detail, Fig. 9 plots zoomed in views of the left side of the flame for the gain minimum when $f\tau_3 = 1.57$ (*a-c*) and the gain maximum when $f\tau_3 = 2.04$ (*d-f*). The images show the mean HRR $\bar{q}_z$ (*left column*), as well as the magnitude and phase of the Fourier mode $\hat{q}_z$ (*middle and right columns*). The mean flame is very similar for both frequencies and most of the HRR occur at the center of the flame brush at $x/d_b \approx 1$. Most of the HRR oscillations displayed in b) and e) occur at the tip of the flame at $x/d_b \approx 1.4$. The phase in Figs. 9 c) and f) shows an approximately linear development downstream ($x-$direction) and is approximately constant along the radius indicative of convective propagation where the convective wavelength can be estimated as $\lambda^{-1} \approx \partial(\angle\tilde{q}_z/2\pi)/\partial x$. However, the phase at the base and the rate of development are noteably different. If the disturbance originated from a single source, the convective wavelength would be expected to be $\lambda \approx \bar{u}/f$. In the case of $f\tau_3 = 2.04$, $\partial(\angle\tilde{q}_z/2\pi)/\partial x$ is significantly smaller resulting in a longer convective wavelength compared to when $f\tau_3 = 1.57$. Changes in the convective wavelength result from superposition of the convective and acoustic sources resulting in a significantly different level of stream-wise interference along the flame front. As shown by the Nyquist plots in Fig. 6, the two sources act in phase at $f\tau_3 = 2.04$, leading to more regular fluctuations in the HRR and a longer convective wavelength. At $f\tau_3 = 1.57$, the two sources are half-a-cycle out of phase along the flame front, leading to destructive interference and a shorter convective wavelength.

4.2. Characterization of stream-wise interference

Given that Fig. 9 showed that the phase mainly develops linearly in the stream-wise direction, we can therefore analyse the

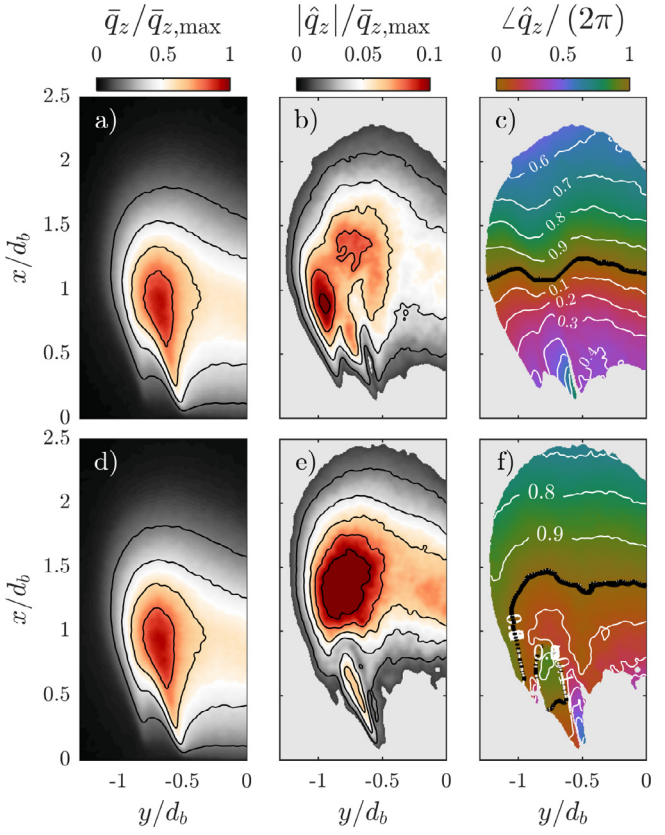

Fig. 9. Structure of: (*left column*) mean HRR $\bar{q}_z$, (*middle column*) the magnitude and (*right column*) phase of the Fourier mode $\hat{q}_z$, at $f\tau_3 = 1.57$ a-c) and $f\tau_3 = 2.04$ d-f). Despite an increase in the forcing frequency, a decrease in the convective wavelength is observed.

interference using line-averaged quantities evaluated in the x-direction only. We can show the effect of $f\tau_3$ on the level of stream-wise interference, following a similar approach to Palies et al. [17] and Wang et al. [40] who divided the flame image into different regions to analyse phase variations in the fluctuating HRR between the different flame regions. We also did the same analysis using the flame surface from the OH-PLIF measurements which yielded a very similar result (not shown for brevity).

Figure 10 plots the line averaged fluctuations in the HRR $\langle q'_{yz}\rangle$ over the oscillation cycle where the vertical axis is the non-dimensional cycle time t/T and the horizontal axis the stream-wise position. Maximum destructive interference resulting in a gain minimum occurs when $f\tau_3 = 1.57$ is shown by the multiple transitions from red-blue-red or vice-versa along a constant t/T. Maximum constructive interference leading to a maximum in gain, occurs when only a single colour is present along a constant t/T as found when $f\tau_3 = 1.8 - 2.04$.

We can further elucidate the nature of the convective-acoustic interference by calculating a stream-wise interference index R which evaluates how the fluctuations in HRR are in phase with itself when integrated over space in a similar way to Wang et al. [40]. To construct R, two scalars $\mathscr{Q}_1$ and $\langle Q'\rangle_{\max}$, are defined as follows:

$$\mathscr{Q}_1 = \int_0^\infty \left|\hat{q}_{yz}\right| \,\mathrm{d}x\,, \tag{6a}$$

$$\langle Q'\rangle_{\max} = \max_{t/T}\left(\int_0^\infty \langle q'_{yz}\rangle \,\mathrm{d}x\right). \tag{6b}$$

$\mathscr{Q}_1$ is the area under the envelope of $\langle q'_{yz}\rangle$ (which are shown by dashed lines in Fig. 11). This provides a measure of the maximum

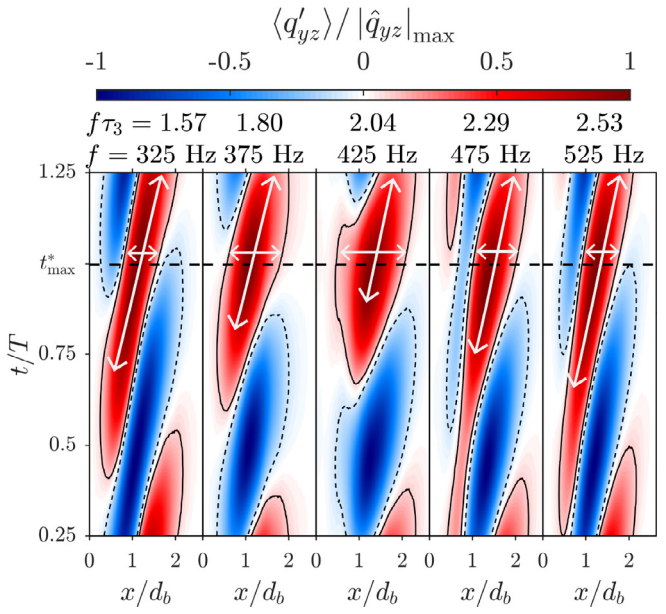

Fig. 10. Evolution of the phase averaged fluctuations of stream-wise HRR $\langle q'_{yz}\rangle$ at different $f\tau_3$. Each panel shows how the fluctuations are distributed in time and space simultaneously. The white arrows indicate the orientation and the convective wavelength of the regions of positive fluctuations, as they change with the forcing frequency. (For interpretation of the references to colour in their figure legend, the reader is referred to the web version of this article.)

amplitude of the integrated fluctuations, in the absence of spatial interference, i.e. neglecting the effect of a non-uniform phase. The second scalar $\langle Q'\rangle_{\max}$, is a measure of the phase-averaged integrated response $\langle Q'\rangle$, when the effect of the non-uniform phase is considered. We condition at $t/T = 1 = t^*_{\max}$ to investigate the interference when the cycle is at maximum HRR at $t^*_{\max}$ as shown in Fig. 10.

Figure 11 a) shows a graphical representation of the two scalars $\mathscr{Q}_1$ and $\langle Q'\rangle_{\max}$ at $f\tau_3 = 1.57$. The area under the dashed black curve A + C, represents the measure $\mathscr{Q}_1$. The area under the dash-dotted red curve A − B, represents the measure $\langle Q'\rangle_{\max}$. Since $\langle Q'\rangle_{\max} \leq \mathscr{Q}_1$ we can define an interference index as:

$$R = \frac{\langle Q'\rangle_{\max}}{\mathscr{Q}_1} \leq 1 \tag{7}$$

which quantifies the effect of the spatial variation of the phase on the integrated amplitude. With $R \approx 0$, the effect of spatial interference is large and in the limit $R = 1$ the effect is negligible.

Figure 11 a) shows regions of positive ($0.7 < x/d_b < 1.5$) and negative ($0 < x/d_b < 0.7$ and $1.5 < x/d_b < 2.3$) fluctuations leading to destructive stream-wise interference and a gain minimum for $f\tau_3$. When $f\tau_3$ is increased, the amount of interference reduces before increasing again. At $f\tau_3 = 2.04$, there is minimal interference and cancellation. However, as $f\tau_3 > 2.04$ regions of negative fluctuations appear again leading to some global cancellation. In Fig. 10 these trends are indicated by the white arrows whose lengths indicate a change of the convective wavelength. The horizontal arrow gets longer from $f\tau_3 = 1.57$ to $f\tau_3 = 2.04$, while the vertical arrow gets shorter. The stream-wise alignment at $f\tau_3 = 2.04$, represented by longer horizontal arrows, results in more constructive interference, and shows a spatial localization of the positive fluctuations. The opposite is observed at $f\tau_3 = 1.57$ and $f\tau_3 = 2.53$, where the fluctuations are more vertically aligned, represented by longer vertical arrows.

We can compare the interference index R to the gain modulations in the FTF by considering the relative change of the different

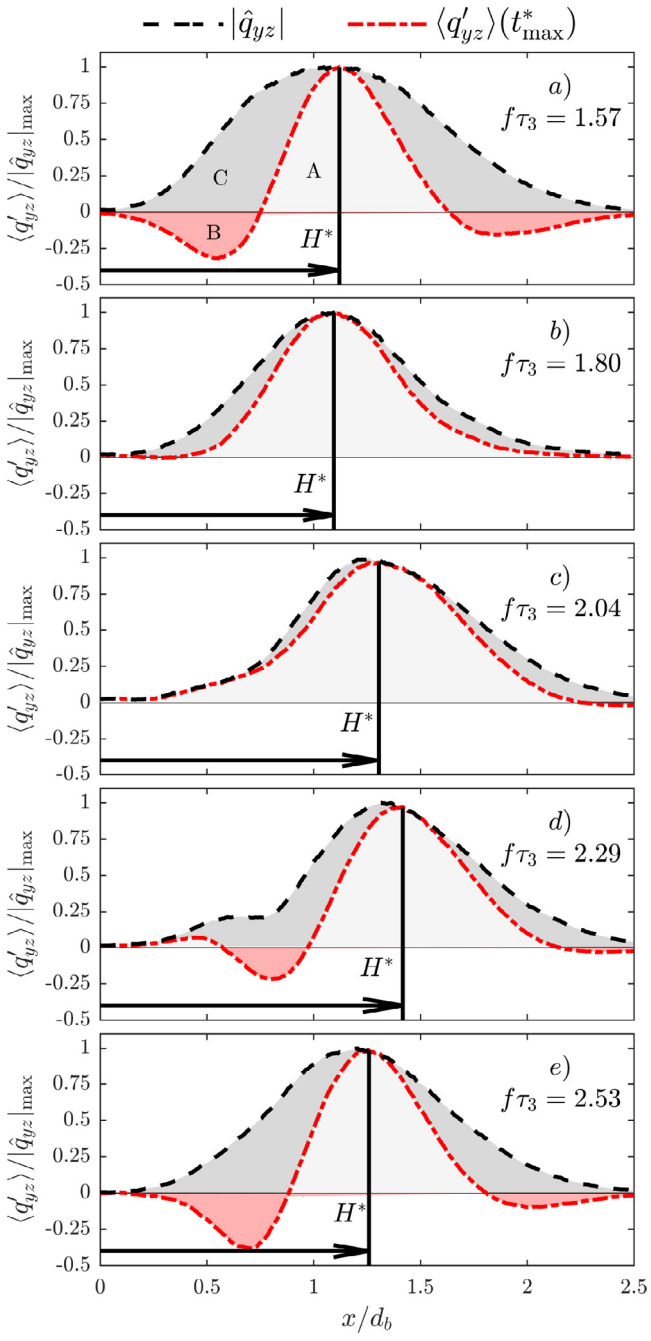

Fig. 11. Phase averaged fluctuations $\langle q'_{yz}\rangle$ shown at $t^*_{\max}$ (along horizontal lines in Fig. 10) and the corresponding envelope $|\hat{q}_{yz}|$ illustrating the metric for stream-wise interference. The area under $|\hat{q}_{yz}|$ corresponds to the first scalar, $\mathscr{Q}_1 = A + C$. The area under $\langle q'_{yz}\rangle$ corresponds to the second scalar, $\langle Q'\rangle_{\max} = A - B$, which gives the global fluctuation in HRR. The modified flame length is estimated as $H^* = \max_x\left(\langle q'_{yz}\rangle\right)$.

quantities. The relative change of interference is given by:

$$\frac{\Delta R}{R} = \frac{R}{\bar{R}} - 1. \tag{8}$$

For the FTF the relative change of gain due to the modulations is given for the DTL model and measurements by:

$$\frac{\Delta G_{\mathrm{DTL}}}{G} = \left|\frac{\mathrm{DTL_T}}{\mathrm{DTL_1}}\right| - 1, \quad \frac{\Delta G_{\mathrm{Exp}}}{G} = \left|\frac{\mathrm{FTF_{Exp}}}{\mathrm{DTL_1}}\right| - 1. \tag{9}$$

The two quantities, $\Delta R/R$ and $\Delta G/G$, are shown in Fig. 12 a). Both quantities form a very similar interference pattern showing

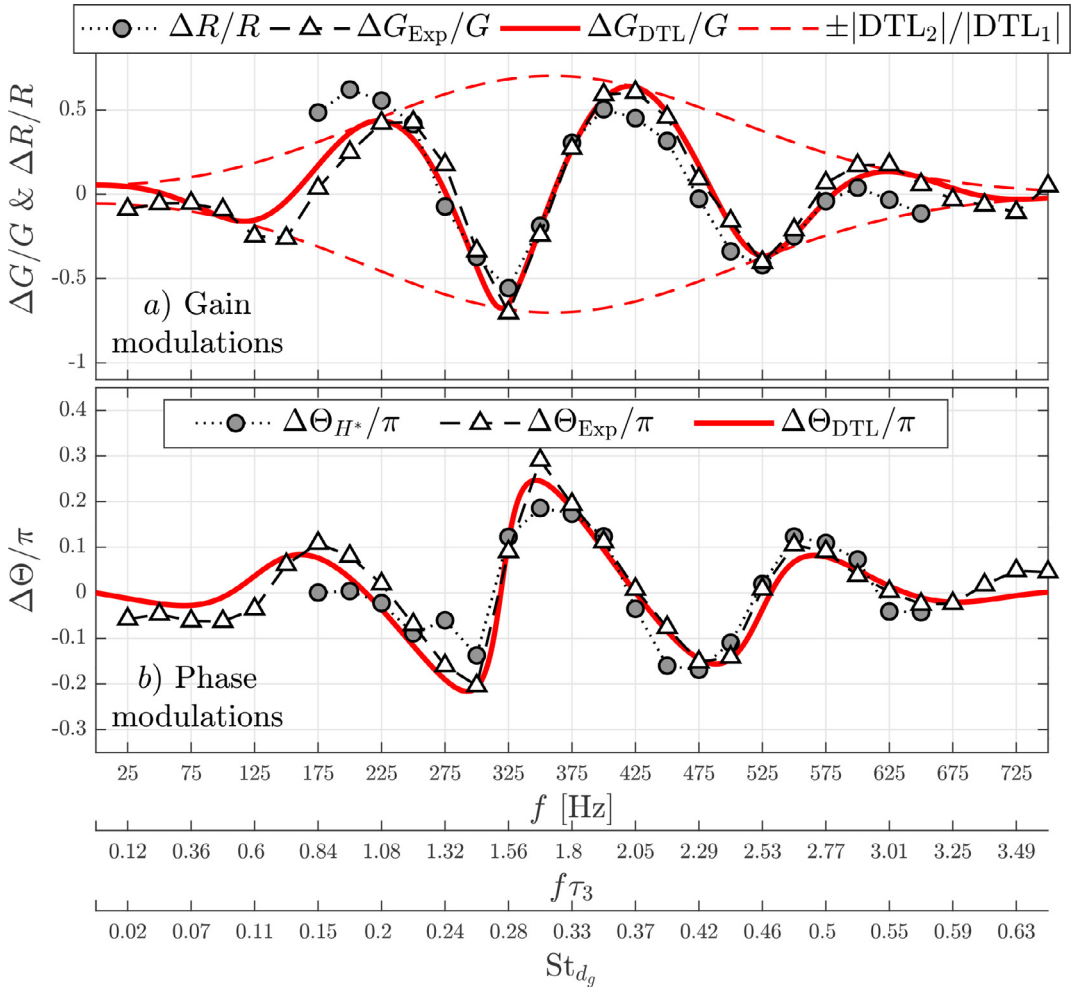

Fig. 12. a) Comparison between the modulations of gain $\Delta G/G$ and the change of the stream-wise interference index $\Delta R/\bar{R}$. The close comparison shows that the modulations in the FTF gain are caused by an equal change in the level of spatial interference, caused by acoustic/convective interference along the flame front. b) Comparison of the relative change of the phase $\Delta\Theta/\pi$, estimated from the FTF and from the characteristic length H^*.

good collapse demonstrating that the change of global HRR which appear as modulations in the FTF gain G are driven by stream-wise interference. It further emphasises the linear interaction in the form of superposition of the convective-acoustic sources along the flame front which determines the global response in HRR. The range of frequencies (or time delays $f\tau_3$) where the band pass filter is active is given by the envelope, $|\mathrm{DTL}_2|/|\mathrm{DTL}_1|$, indicated by the red dashed line in Fig. 12 a) which is centered on the natural shedding frequency of the cylinders at $\mathrm{St}_{d_g} = 0.3$.

In Fig. 11 we can define a distance H^* from the dump plane to the peak HRR in the stream-wise direction, $\max_x(\langle q'_{yz}\rangle)$. The distance H^* varies with the forcing frequency and differs from H used as the characteristic length in the Strouhal number scaling for the cut-off frequency which was based on the mean flame images ($\max_x(\bar{q}_{yz})$) not the Fourier quantities. The change in H^* leads to a change in the phase $\Delta\Theta$ and can be estimated by:

$$\Delta\Theta_{H^*} = \frac{-2\pi\left(H^* - \bar{H}^*\right)f}{\bar{u}}, \tag{10}$$

where $\bar{H}^*/\bar{u}$ represents the average time-delay. From the DTL model and FTF measurements, the change of the phase is given by:

$$\Delta\Theta_{\mathrm{DTL}} = \angle\left(\frac{\mathrm{DTL_T}}{\mathrm{DTL_1}}\right), \quad \Delta\Theta_{\mathrm{Exp}} = \angle\left(\frac{\mathrm{FTF_{Exp}}}{\mathrm{DTL_1}}\right). \tag{11}$$

The various ways to calculate $\Delta\Theta$ are plotted in Figure 12 b) showing a good collapse and that the phase is modulated within the same band of frequencies as the gain modulations in a). It also demonstrates that:

1. The characteristic length H^* obtained from fluctuating quantities provides a good estimate of the total time delay/phase from the global measurements. Usually this length is taken to be H from the mean flame images which has been shown to only provide a good estimate for the mean time delay [15].
2. The interference is a linear phenomenon. The DTL model assumes a linear superposition of convective and acoustic sources by construction and it provides an excellent representation of the global behaviour. As the relative time-delay between the two sources represented by $f\tau_3$ changes, the characteristic length H^* also shifts accordingly, which leads to a change of the global time-delay observed in the phase of the FTF.

4.3. Flame sheet kinematics

In this section we draw a link between the constructive and destructive interference observed in the global HRR response to the local flame statistics and dynamics. To do this we compute the flame curvature from the flame surface coordinates $(x_s(l_s), y_s(l_s))$ which are parameterized by the arc length l_s. The flame curvature gives the local rate of change of direction of the flame front

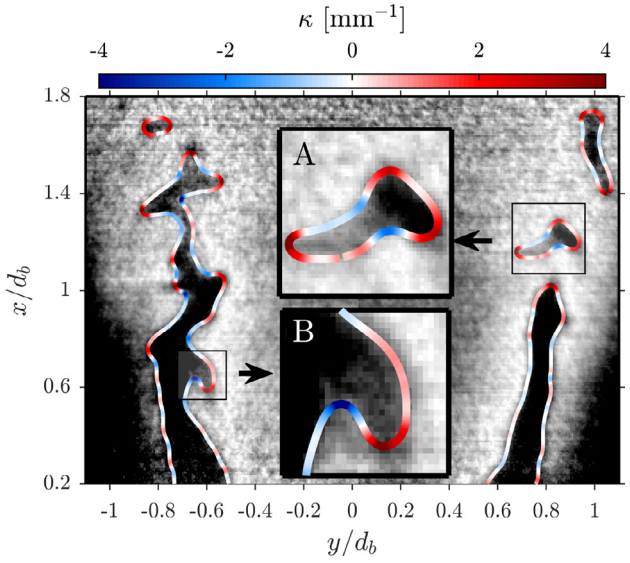

Fig. 13. Snapshot of an OH*-PLIF image and the flame surface (X_s, Y_s) for the unforced flame. The flame surface is coloured by curvature κ. The two boxes labeled A and B indicate two features along the flame front. A) shows flame pinch-off which has a preference for positive curvature. B) shows flame front wrinkling which has a preference for both positive and negative curvature.

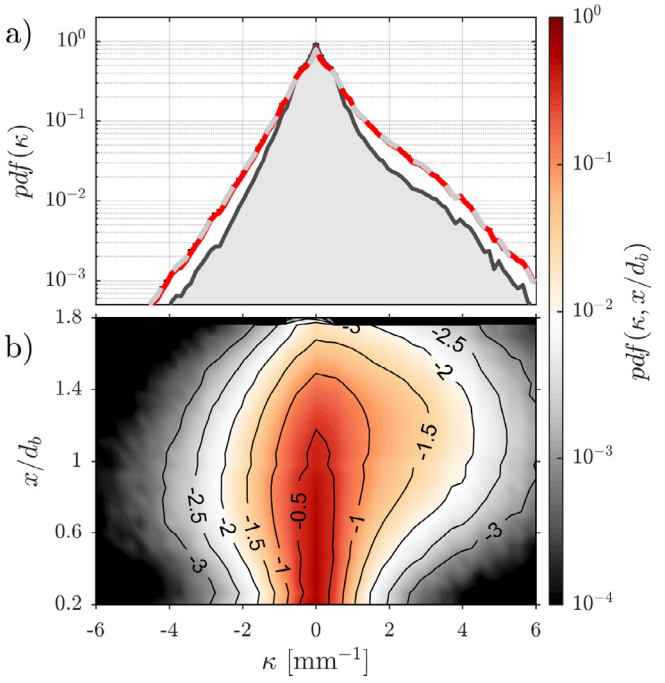

Fig. 14. a) PDFs ($pdf(\kappa)$) of curvature for $f\tau_3 = 1.57$ (—), $f\tau_3 = 2.04$ (—), and the unforced flame (—). Acoustic forcing increases the total magnitude of curvature but is very similar for both frequencies. b) Joint PDFs ($pdf(\kappa, x/d_b)$) of curvature and stream-wise position shown for $f\tau_3 = 2.04$.

but can also be used to quantify dynamic features along the flame front, such as vortex roll-up and flame pinch off. Curvature is computed using the approach of [41] and is briefly explained here. By convolving each coordinate along an open or closed flame curve by a kernel, $h(l_s)$, the gradients of the smoothed coordinates (X_s, Y_s) are (for x_s only for brevity):

$$X_s = x_s * h, \qquad \dot{X}_s = x_s * \dot{h}, \qquad \ddot{X}_s = x_s * \ddot{h}, \tag{12}$$

where the dot denotes a derivative with respect to the arc length, $\dot{X}_s = \partial X_s / \partial l_s$. The kernel $h(l_s)$ was chosen to be a Gaussian PDF which is sampled with $n_p = 25$ equidistant points in the region $l_s = [-5\sigma_p,\ 5\sigma_p]$, where σ_p is the standard deviation. In this way h is a weighting function whose sum equals to unity, and thus Eq. (12) can be considered a weighted average operator over n_p neighbouring points. The quantities in Eq. (12) are computed and the curvature κ for the smoothed curve (X_s, Y_s) is given by:

$$\kappa = \frac{\dot{X}_s \ddot{Y}_s - \dot{Y}_s \ddot{X}_s}{\left[\dot{X}_s^2 + \dot{Y}_s^2\right]^{3/2}}, \tag{13}$$

where κ is positive when the flame concave towards the unburnt reactants and negative when it convex towards the unburnt reactants.

Figure 13 shows a snapshot of an instantaneous PLIF image where the flame surface (X_s, Y_s) is shown colored by curvature κ. The insets in the figure labeled A and B show zoomed areas of two characteristic features tracked by curvature. Inset A shows a pocket of unburned gas that has pinched-off from the main flame and curves in towards the reactants. This increases the amount of positive curvature. Inset B shows a typical wrinkle along the flame front typical of vortex roll-up, which leads to an increase of both positive and negative curvature.

We first consider the statistics of the local flame curvature to identify any effect of acoustic forcing. The Probability Density Function (PDF) of κ is shown in Fig. 14 a) for the unforced flame and two different $f\tau_3$. A non-Gaussian distribution is observed with longer tails for positive κ for the forced and unforced flames. Overall, the forced flames exhibit longer tails for both positive and negative κ compared to the unforced flame. This indicates that forced flames exhibit an increase curvature over all length-scales leading to more contorted flames. The PDFs for the two frequencies are also very similar, suggesting that the overall increase in curvature of the forced flames may only weakly depend on frequency.

Figure 14 b) plots the joint PDF of κ with stream-wise position x/d_b for $f\tau_3 = 2.04$ showing the spatial evolution of the curvature probability. Both frequencies displayed very similar distributions, hence only a single case is presented. Close to the flame base the PDF is reasonably symmetric reflecting the low level of flame wrinkling near the flame base. The PDF becomes increasingly skewed downstream as the variance of the PDF becomes wider for positive κ. The increased probability in positive κ is expected to result from the effect of vortex roll-up from acoustic forcing. The maximum positive κ occurs near the tip of the flame, i.e. $x/d_b > 0.8$, which indicates that consumption of pockets due to flame pinch-off, as shown in A of Fig. 13, is dominant in this region as shown previously [35,42–44].

More insight in the flame dynamics can be obtained by considering the phase-averaged curvature. Figure 15 compares phase-averaged curvature $\langle|\kappa|_{xy}\rangle$, flame surface $\langle s_{xy}\rangle$, and HRR $\langle Q\rangle$ plotted over two cycles. The global fluctuations of HRR and flame surface are in phase with each other for both frequencies as expected. Due to the different convective-acoustic interference, the amplitude of $\langle Q\rangle$ for $f\tau_3 = 1.57$ in a) is significantly lower than $f\tau_3 = 2.04$ shown in b). However, the opposite trend is found for the amplitude of curvature $\langle|\kappa|_{xy}\rangle$ which is larger for $f\tau_3 = 1.57$. Furthermore, there is also a difference in the phase with $\langle Q\rangle$ and $\langle|\kappa|_{xy}\rangle$ by half a cycle for $f\tau_3 = 1.57$ and under a quarter of a cycle for $f\tau_3 = 2.04$.

To further elucidate differences in the flame response between the two frequencies, the spatial response of the phase-averaged fluctuation of curvature in the form of joint PDFs of the phase-averaged fluctuations of curvature $\langle\kappa'\rangle$ and stream-wise position x/d_b, $pdf(\langle\kappa'\rangle, x/d_b)$ are plotted in Fig. 16. The figure shows half of a forcing cycle with the top and bottom rows corresponding to $f\tau_3 = 1.57$ and 2.04 respectively. The figure shows the probability

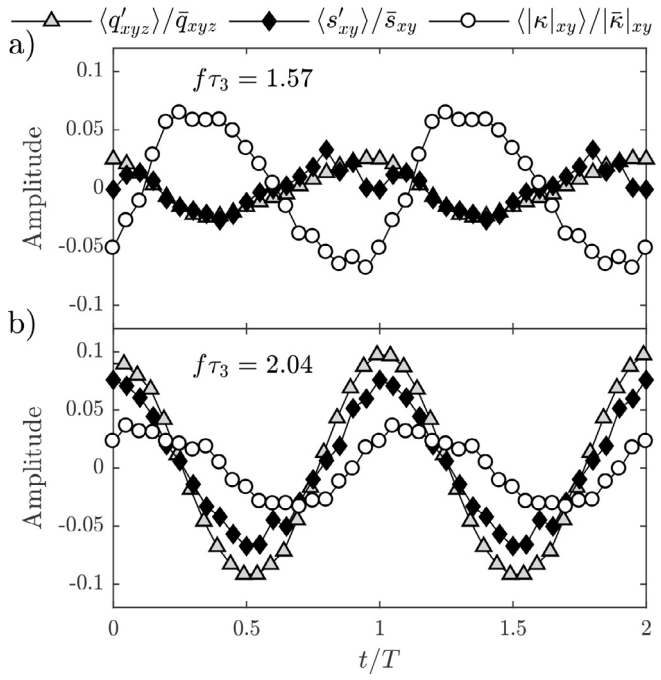

Fig. 15. Phase averaged fluctuations of global HRR $\langle Q\rangle$ (⊛) flame surface $\langle s_{xy}\rangle$ (●) and curvature $\langle|\kappa|_{xy}\rangle$ (○) shown at a) $f\tau_3 = 1.57$, and b) $f\tau_3 = 2.04$. At $f\tau_3 = 1.57$, the fluctuations of curvature is half a cycle out of phase with the HRR and flame surface. At $f\tau_3 = 2.04$, the fluctuations of curvature are more in phase with the HRR and flame surface.

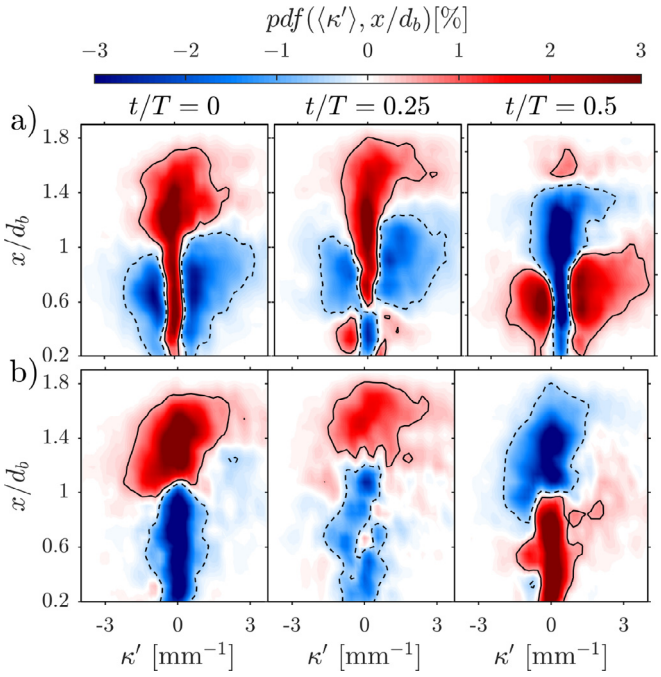

Fig. 16. joint PDF of the phase averaged fluctuations of curvature and stream-wise position $pdf(\langle\kappa'\rangle, x/d_b)$ shown through half a cycle for a) $f\tau_3 = 1.57$ and b) $f\tau_3 = 2.04$.

of the fluctuations in curvature above and below the mean curvature. Therefore zero (white) values of the colour bar is the mean curvature and the positive (red) and negative (blue) values represent variations about the mean.

Both frequencies show a relatively sharp change in the distributions upstream and downstream of $x/d_b = 1$. Beginning with $f\tau_3 = 1.57$ at $t/T = 0$, upstream the probability of curvature fluctuations is very low illustrated by both the narrow red band of high probability centred on $\kappa' \approx 0$ surrounded by blue regions of low probability. Downstream beyond $x/d_b > 1$, a high probability of curvature fluctuations (both positive and negative) is observed by the large red area which corresponds to the flame tip region which shortly pinches-off. This corresponds to minimum curvature and maximum HRR as shown in Fig. 15. A similar distribution is found at $t/T = 0.25$ except below $x/d_b < 0.5$ where the probability distribution has reversed: the probability has decreased along $\kappa' = 0$ but increased for $|\kappa'| > 0$ shown by the blue and red bands. This corresponds to the start of the periodic vortex-flame roll-up whereas the high probability of region downstream $x/d_b > 1$ is due to the large-scale pinch-off of the flame front that leads to pocket formation. When $t/T = 0.5$, the probability distribution is almost the inverse of $t/T = 0$ with upstream flame now strongly wrinkled due to vortex-flame interaction but having low probability (blue) of curvature fluctuations downstream as the flame pockets have advected and burned out.

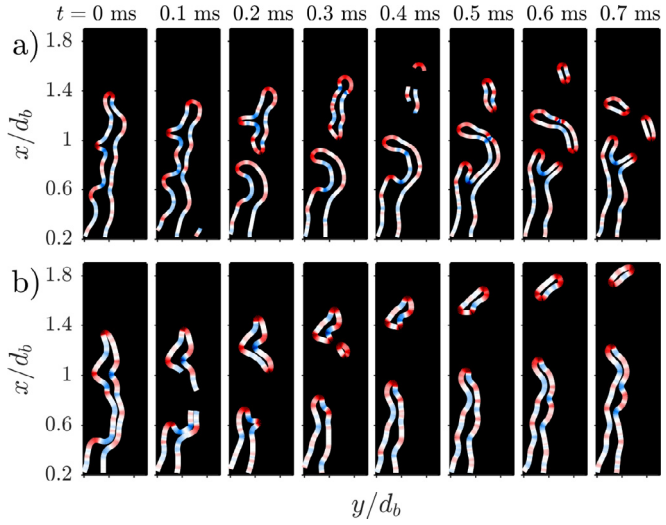

Fig. 17. Time-series of the instantaneous flame surface (X_s, Y_s) colored by curvature κ for a) $f\tau_3 = 1.57$ and b) $f\tau_3 = 2.04$.

The corresponding flame dynamics leading to these PDFs are shown in Fig. 17 a). At $t = 0$ms the overall curvature along the flame front is increasing resulting in pinch-off of the flame front at $x/d_b \approx 1$ and large-scale hook-shaped deformation of the flame. As the pocket advects downstream and burns out, a second pocket is formed leaving a highly contorted forked flame tip. The second pocked then divides into two. Overall, the process shows that although the flame dynamics lead to high levels of curvature/deformation where the destruction of flame surface area by multiple pocket burnout downstream is counteracted by the simultaneous increase in the flame surface due to wrinkling upstream. These out-of-phase contributions lead to the reduction in the amplitude in the HRR observed in Figure 15.

The curvature of the flame is comparatively reduced when $f\tau_3 = 2.04$ in Fig. 16 b). As observed in a) there is a sharp change in the probability distribution upstream and downstream of $x/d_b = 1$. However, the upstream region now shows a much lower probability of κ' as shown by the narrower blue and red regions centred along $\kappa' = 0$. At $t/T = 0$ a narrow low probability of $\kappa' = 0$ indicates the flame experiences a relatively low level of wrinkling upstream but a high level of wrinkling downstream in the region of the flame tip which is about to pinch off. Similar distributions are observed at $t/T = 0.25$ but with lower values. At $t/T = 0.5$, again the probability distribution is almost the inverse of $t/T = 0$ with upstream having high probability centred $\kappa' = 0$ and a low prob-

ability (blue) of curvature fluctuations downstream as the flame pockets have advected and/or burned out. The PDFs show lower overall probability of curvature fluctuations than a).

The lower overall curvature can be observed in the corresponding flame dynamics in Fig. 17 b). Once pinch-off occurs around $t = 0.1$ms and forms a pocket which advects and burns out downstream, the flame upstream increases in surface area but is significantly less contorted than the flame in sequence a). The main difference with the flame dynamics $f\tau_3 = 1.57$ is that there is only one pinch-off event and pocket burnout, compared with multiple pocket formations and burnout in a), and therefore a larger relative production in flame surface occurs via the wrinkling of the flame front upstream.

5. Conclusions

This paper presented a method which can be used to passively modulate the gain and phase of FTFs of bluff-body stabilized CH_4/H_2 flames by controlling the interference between convective and acoustic disturbances through careful scaling of relative time delays. Convective disturbances were produced by several different upstream geometries: a set of three small diameter cylinders, three streamlined bodies (Rankine ovals) and a six-vaned swirler which were placed upstream at two different locations. Modulations in the gain were produced for all geometries demonstrating that their physical origin is the vortex/wake shedding (locked on to the forcing frequency) which scales with $\mathrm{St}_{d_g} = fd_g/\bar{u}_p$ where d_g is the characteristic length of the upstream geometry (e.g. the diameter of the cyclinder) and $\bar{u}_p$ the approach velocity. The different upstream geometries produce different modulation wavelengths which scale with the time-delay, $\tau_3 = L_g/\bar{u}_p$ where L_g is distance from the upstream geometry to the flame base. The global flame response was shown to result from a linear superposition of convective-acoustic disturbances which can be controlled by the relative time-delay, τ_3. The underlying scalings and time delays of the convective-acoustic interference are shown to be well modelled using a distributed time-lag (DTL) model which can also be used to tune and optimise the convective-acoustic interference. Using the DTL model to control the convective-acoustic interference the following steps are required (for cylinders):

1. The diameter of the cylinders, d_g, should be chosen such that $\mathrm{St}_{d_g} = [0.2 \text{ to } 0.4]$ for a target mass flow and frequency range. This ensures the frequency range to be controlled is close to the natural shedding frequency of the cylinders to ensure lock-on.
2. The relative time-delay is then changed by placing the upstream geometry at an upstream distance L_g from the flame such that the gain parameters g_1 and g_2 are of a similar order of magnitude.
3. To obtain large phase modulations at a given frequency L_g should be chosen in intervals of $\pi/2$ such that $f\tau_3 = fL_g/\bar{u}_p = [0.75, 1.25, 1.75]$.
4. To obtain large gain suppression at a given frequency L_g should be chosen in intervals of π such that $f\tau_3 = [0.5, 1.5, 2.5]$.

The second part of the paper show how the convective-acoustic interference affects the flame dynamics. The modulations in the gain are accompanied by stream-wise interference of HRR and flame surface fluctuations which change the integrated magnitude and the characteristic length of the flame. At frequencies of destructive interference, an increase of flame surface due to flame vortex roll-up occurs simultaneously as flame surface is annihilated at the tip of the flame due to multiple pinch off events. At frequencies of constructive interference the increase of flame surface due to the two mechanisms, i.e. flame vortex roll-up and flame pinch off, occur in phase, leading to an increase in the global HRR. Despite the small magnitude of these coherent oscillations on a turbulent flame, the role of the forcing is not to result in larger scale pinch off or significantly stronger wrinkling, but to synchronise the occurrence of wrinkling, pinch off, pocket formation and burnout resulting in the global flame response observed as modulations in the FTF.

Declaration of Competing Interest

The authors declare that they have no known competing financial interests or personal relationships that could have appeared to influence the work reported in this paper.

Acknowledgments

The authors acknowledge support from the NCCS Centre, funded under the Norwegian research program, Centres for Environment-friendly Energy Research (FME). Grant no.: 257579/E20. This work was also supported by the European Research Council (ERC) under the European Union's Horizon 2020 research and innovation programme (grant agreement no 677931 TAIAC).

Appendix A. Phase average and Fourier mode analysis

When investigating the response of the flame to harmonic oscillations it is useful to compute phase averaged quantities. For a given quantity, e.g. q_z, the phase averaged is denoted by brackets as $\langle q_z \rangle$ and is decomposed as:

$$\langle q_z \rangle = \bar{q}_z + \langle q_z' \rangle \,, \tag{A.1}$$

where $\langle q_z' \rangle$ is the phase averaged fluctuation of q_z' obtained by conditional averaging on the cycle phase.

The amplitude and phase of the fluctuations are also estimated from the Fourier modes which are obtained from spectral analysis similar to [45,46]. For the images each camera pixel is treated as individual time-series. Then, the spatial distribution of the amplitude and phase, represented by $\hat{q}_z$, is computed similar to the method outlined in Eq. (2) by computing the PSD. $\hat{q}_z$ only contains information at a specific frequency, which is chosen to be the external excitation frequency f. Hence, harmonics of f are discarded. When $\hat{q}_z$ is known, $\langle q_z' \rangle$ is given by:

$$\langle q_z' \rangle (x, y, t) = \mathrm{Re}\left\{ \hat{q}_z(x, y) \exp\left(2\pi j \frac{t}{T} \right) \right\}. \tag{A.2}$$

Similarly, Eq. (A.1) and Eq. (A.2) are used to obtain the other quantities, e.g. the phase averaged flame surface $\hat{s}$. The phase reference of all hatted quantities ($\hat{\cdot}$) is chosen so that $t/T = 0$ occurs at peak HRR, i.e. at $\max_t(\langle q_{xyz}' \rangle)$. This phase instance is denoted as $t^*_{\max}$.

References

[1] T.C. Lieuwen, V. Yang, Combustion instabilities in gas turbine engines: Operational experience, fundamental mechanisms, and modeling, AIAA, Reston,VA, 2006.
[2] A. Gruber, M.R. Bothien, A. Ciani, K. Aditya, J.H. Chen, F.A. Williams, Direct Numerical Simulation of hydrogen combustion at auto-ignitive conditions: Ignition, stability and turbulent reaction-front velocity, Combust. Flame 229 (2021) 111385, doi:10.1016/j.combustflame.2021.02.031.
[3] M.R. Bothien, A. Ciani, J.P. Wood, G. Fruechtel, Toward decarbonized power generation with gas turbines by using sequential combustion for burning Hydrogen, J. Eng. Gas Turb. Power 141 (12) (2019), doi:10.1115/1.4045256.
[4] T. Schuller, T. Poinsot, S. Candel, Dynamics and control of premixed combustion systems based on flame transfer and describing functions, J. Fluid Mech. 894 (2020) P1, doi:10.1017/jfm.2020.239.
[5] J.W. Strutt, The theory of sound, 2nd ed, Dover, New York, NY, 1945.
[6] C. Külsheimer, H. Büchner, Combustion dynamics of turbulent swirling flames, Combust. Flame 131 (1) (2002) 70–84, doi:10.1016/S0010-2180(02)00394-2.
[7] D. Durox, T. Schuller, N. Noiray, S. Candel, Experimental analysis of nonlinear flame transfer functions for different flame geometries, Proc. Combust. Inst. 32 (1) (2009) 1391–1398, doi:10.1016/j.proci.2008.06.204.

[8] K.T. Kim, J.G. Lee, B.D. Quay, D.A. Santavicca, Response of partially premixed flames to acoustic velocity and equivalence ratio perturbations, Combust. Flame 157 (9) (2010) 1731–1744, doi:10.1016/j.combustflame.2010.04.006.
[9] P. Palies, D. Durox, T. Schuller, S. Candel, Nonlinear combustion instability analysis based on the flame describing function applied to turbulent premixed swirling flames, Combust. Flame 158 (10) (2011) 1980–1991, doi:10.1016/j.combustflame.2011.02.012.
[10] A. Kaufmann, F. Nicoud, T. Poinsot, Flow forcing techniques for numerical simulation of combustion instabilities, Combust. Flame 131 (4) (2002) 371–385, doi:10.1016/S0010-2180(02)00419-4.
[11] T. Schuller, D. Durox, S. Candel, A unified model for the prediction of laminar flame transfer functions: comparisons between conical and V-flame dynamics, Combust. Flame 134 (1) (2003) 21–34, doi:10.1016/S0010-2180(03)00042-7.
[12] W. Polifke, C. Lawn, On the low-frequency limit of flame transfer functions, Combust. Flame 151 (3) (2007) 437–451, doi:10.1016/j.combustflame.2007.07.005.
[13] A.P. Dowling, A kinematic model of a ducted flame, J. Fluid Mech. 394 (1999) 51–72, doi:10.1017/S0022112099005686.
[14] M. Fleifil, A.M. Annaswamy, Z.A. Ghoneim, A.F. Ghoniem, Response of a laminar premixed flame to flow oscillations: A kinematic model and thermoacoustic instability results, Combust. Flame 106 (4) (1996) 487–510, doi:10.1016/0010-2180(96)00049-1.
[15] E. Æsøy, J.G. Aguilar, S. Wiseman, M.R. Bothien, N.A. Worth, J.R. Dawson, Scaling and prediction of transfer functions in lean premixed H2/CH4-flames, Combust. Flame 215 (2020) 269–282, doi:10.1016/j.combustflame.2020.01.045.
[16] T. Komarek, W. Polifke, Impact of swirl fluctuations on the flame response of a perfectly premixed swirl burner, J. Eng. Gas Turb. Power 132 (6) (2010), doi:10.1115/1.4000127.
[17] P. Palies, D. Durox, T. Schuller, S. Candel, The combined dynamics of swirler and turbulent premixed swirling flames, Combust. Flame 157 (9) (2010) 1698–1717, doi:10.1016/j.combustflame.2010.02.011.
[18] M. Gatti, R. Gaudron, C. Mirat, L. Zimmer, T. Schuller, A comparison of the transfer functions and flow fields of flames with increasing swirl number, ASME, 2018.
[19] F. Di Sabatino, T.F. Guiberti, W.R. Boyette, W.L. Roberts, J.P. Moeck, D.A. Lacoste, Effect of pressure on the transfer functions of premixed methane and propane swirl flames, Combust. Flame 193 (2018) 272–282, doi:10.1016/j.combustflame.2018.03.011.
[20] H.T. Nygård, N. Worth, Flame transfer functions and dynamics of a closely confined premixed body stabilised flame with swirl, J. Eng. Gas Turb. Power (2021), doi:10.1115/1.4049513.
[21] W. Polifke, Black-box system identification for reduced order model construction, Ann. Nucl. Energy 67 (2014) 109–128, doi:10.1016/j.anucene.2013.10.037.
[22] P. Palies, D. Durox, T. Schuller, S. Candel, Experimental Study on the Effect of Swirler Geometry and Swirl Number on Flame Describing Functions, Combust. Sci. Technol. 183 (7) (2011) 704–717, doi:10.1080/00102202.2010.538103.
[23] P. Palies, D. Durox, T. Schuller, S. Candel, Acoustic-convective mode conversion in an aerofoil cascade, J. Fluid Mech. 672 (2011) 545–569, doi:10.1017/S0022112010006142. Publisher: Cambridge University Press
[24] M. Gatti, R. Gaudron, C. Mirat, L. Zimmer, T. Schuller, Impact of swirl and bluff-body on the transfer function of premixed flames, Proceedings of the Combustion Institute 37 (4) (2019) 5197–5204, doi:10.1016/j.proci.2018.06.148.
[25] E. Æsøy, J.G. Aguilar, M.R. Bothien, N. Worth, J. Dawson, Acoustic-Convective interference in transfer functions of Methane/Hydrogen and Pure Hydrogen flames, J. Eng. Gas Turb. Power (2021), doi:10.1115/1.4051960.
[26] W. Polifke, Modeling and analysis of premixed flame dynamics by means of distributed time delays, Prog. Energy Combust. Sci. 79 (2020) 100845, doi:10.1016/j.pecs.2020.100845.
[27] N.A. Worth, J.R. Dawson, Self-excited circumferential instabilities in a model annular gas turbine combustor: Global flame dynamics, Proc Combust Inst. 34 (2) (2013) 3127–3134, doi:10.1016/j.proci.2012.05.061.
[28] A.F. Seybert, D.F. Ross, Experimental determination of acoustic properties using a two-microphone random-excitation technique, The Journal of the Acoustical Society of America 61 (5) (1977) 1362–1370, doi:10.1121/1.381403.
[29] B. Higgins, M.Q. McQuay, F. Lacas, J.C. Rolon, N. Darabiha, S. Candel, Systematic measurements of OH chemiluminescence for fuel-lean, high-pressure, premixed, laminar flames, Fuel 80 (1) (2001) 67–74, doi:10.1016/S0016-2361(00)00069-7.
[30] R. Balachandran, B.O. Ayoola, C.F. Kaminski, A.P. Dowling, E. Mastorakos, Experimental investigation of the nonlinear response of turbulent premixed flames to imposed inlet velocity oscillations, Combust. Flame 143 (1) (2005) 37–55, doi:10.1016/j.combustflame.2005.04.009.
[31] B. Schuermans, F. Guethe, D. Pennell, D. Guyot, C.O. Paschereit, Thermoacoustic modeling of a gas turbine using transfer functions measured under full engine pressure, J. Eng. Gas Turb. Power 132 (11) (2010) 111503, doi:10.1115/1.4000854.
[32] M. Reyes, F.V. Tinaut, B. Giménez, J.V. Pastor, Effect of hydrogen addition on the OH* and CH* chemiluminescence emissions of premixed combustion of methane-air mixtures, Int. J. Hydrog 43 (42) (2018) 19778–19791, doi:10.1016/j.ijhydene.2018.09.005.
[33] W. Rong, Z. Li, W. Zhang, L. Sun, An improved canny edge detection algorithm, 2014 IEEE international conference on mechatronics and automation, IEEE (2014), pp. 577–582.
[34] N.A. Worth, J.R. Dawson, Cinematographic OH-PLIF measurements of two interacting turbulent premixed flames with and without acoustic forcing, Combust. Flame 159 (3) (2012) 1109–1126, doi:10.1016/j.combustflame.2011.09.006.
[35] N.A. Worth, J.R. Dawson, Characterisation of flame surface annihilation events in self excited interacting flames, Combust. Flame 199 (2019) 338–351, doi:10.1016/j.combustflame.2018.10.032.
[36] A. Roshko, On the Development of Turbulent Wakes from Vortex Streets (1954). http://ntrs.nasa.gov/search.jsp?R=19930092207.
[37] A. Albayrak, M.P. Juniper, W. Polifke, Propagation speed of inertial waves in cylindrical swirling flows, J. Fluid Mech. 879 (2019) 85–120, doi:10.1017/jfm.2019.641.
[38] S.B. Pope, Turbulent Flows, Measurement Science and Technology 12 (11) (2001) 2020–2021, doi:10.1088/0957-0233/12/11/705. Publisher: IOP Publishing
[39] O.M. Griffin, M.S. Hall, Review-Vortex shedding lock-on and flow control in bluff body wakes, J. Fluids Eng. 113 (4) (1991) 526–537, doi:10.1115/1.2926511.
[40] G. Wang, T.F. Guiberti, X. Xia, L. Li, X. Liu, W.L. Roberts, F. Qi, Decomposition of swirling flame transfer function in the complex space, Combust. Flame 228 (2021) 29–41, doi:10.1016/j.combustflame.2021.01.032.
[41] F. Mokhtarian, S. Abbasi, Shape similarity retrieval under affine transforms, Pattern Recognition 35 (1) (2002) 31–41, doi:10.1016/S0031-3203(01)00040-1.
[42] A. Tyagi, I. Boxx, S. Peluso, J. O'Connor, The role of flow interaction in flame-flame interaction events in a dual burner experiment, Proc. Combust. Inst. 37 (2) (2019) 2485–2491, doi:10.1016/j.proci.2018.07.036.
[43] A. Tyagi, I. Boxx, S. Peluso, J. O'Connor, Pocket formation and behavior in turbulent premixed flames, Combust. Flame 211 (2020) 312–324, doi:10.1016/j.combustflame.2019.09.033.
[44] A. Tyagi, J. O'Connor, Towards a method of estimating out-of-plane effects on measurements of turbulent flame dynamics, Combust. Flame 216 (2020) 206–222, doi:10.1016/j.combustflame.2020.02.010.
[45] J. O'Connor, V. Acharya, T. Lieuwen, Transverse combustion instabilities: Acoustic, fluid mechanic, and flame processes, Prog. Energy Combust. Sci. 49 (2015) 1–39, doi:10.1016/j.pecs.2015.01.001.
[46] E. Æsøy, J.G. Aguilar, N.A. Worth, J.R. Dawson, The response of an axisymmetric jet placed at various positions in a standing wave, J. Fluid Mech. 917 (2021), doi:10.1017/jfm.2021.246.